

SCIENTIFIC REPORTS



OPEN

Hydrogen separation through tailored dual phase membranes with nominal composition $\text{BaCe}_{0.8}\text{Eu}_{0.2}\text{O}_{3-\delta}:\text{Ce}_{0.8}\text{Y}_{0.2}\text{O}_{2-\delta}$ at intermediate temperatures

Mariya E. Ivanova¹, Sonia Escolástico², Maria Balaguer¹, Justinas Palisaitis³, Yoo Jung Sohn¹, Wilhelm A. Meulenber¹, Olivier Guillon¹, Joachim Mayer³ & Jose M. Serra²

Received: 25 May 2016
Accepted: 19 September 2016
Published: 04 November 2016

Hydrogen permeation membranes are a key element in improving the energy conversion efficiency and decreasing the greenhouse gas emissions from energy generation. The scientific community faces the challenge of identifying and optimizing stable and effective ceramic materials for H_2 separation membranes at elevated temperature (400–800 °C) for industrial separations and intensified catalytic reactors. As such, composite materials with nominal composition $\text{BaCe}_{0.8}\text{Eu}_{0.2}\text{O}_{3-\delta}:\text{Ce}_{0.8}\text{Y}_{0.2}\text{O}_{2-\delta}$ revealed unprecedented H_2 permeation levels of 0.4 to 0.61 mL·min⁻¹·cm⁻² at 700 °C measured on 500 μm-thick-specimen. A detailed structural and phase study revealed single phase perovskite and fluorite starting materials synthesized via the conventional ceramic route. Strong tendency of Eu to migrate from the perovskite to the fluorite phase was observed at sintering temperature, leading to significant Eu depletion of the proton conducting $\text{BaCe}_{0.8}\text{Eu}_{0.2}\text{O}_{3-\delta}$ phase. Composite microstructure was examined prior and after a variety of functional tests, including electrical conductivity, H_2 -permeation and stability in CO_2 containing atmospheres at elevated temperatures, revealing stable material without morphological and structural changes, with segregation-free interfaces and no further diffusive effects between the constituting phases. In this context, dual phase material based on $\text{BaCe}_{0.8}\text{Eu}_{0.2}\text{O}_{3-\delta}:\text{Ce}_{0.8}\text{Y}_{0.2}\text{O}_{2-\delta}$ represents a very promising candidate for H_2 separating membrane in energy- and environmentally-related applications.

Hydrogen permeation membranes are a key element to reach high energy conversion efficiency and decreasing the greenhouse gas emissions from power generation and energy-intensive industries, i.e. by capturing and utilizing CO_2 or moving towards hydrogen-based systems by extracting highly pure H_2 from gas mixtures^{1–3}. In this context, the integration of high performance H_2 -permeation ceramic membranes with competitive manufacturing cost and life time (>3 years) in industrial processes can significantly intensify them by (i) maximizing products yield and energy efficiency and (ii) promoting the reaction rates⁴. Such integrative membrane approach of *in situ* H_2 extraction (used as fuel) or consumption (as raw material for chemical production) in a proton conductor-based membrane reactor would shift the thermodynamic equilibrium towards the product side, hence boosting process efficiency, saving energy and reducing final product cost- all factors of high environmental and economic impact. Proton conducting ceramic membranes may therefore be of interest for integrated gasification process^{5,6}, and more specifically in water gas shift reactors at elevated temperatures (600–900 °C)⁷, in catalytic membrane reactors (CMRs) for accomplishing chemical and petro-chemical reactions (e.g. ammonia synthesis^{8,9}, non-oxidative de-hydrogenation reaction¹⁰).

¹Institute of Energy and Climate Research IEK-1, Forschungszentrum Jülich GmbH, D-52425 Jülich, Germany.

²Instituto de Tecnología Química, Universidad Politécnica de Valencia-Consejo Superior de Investigaciones Científicas, Av. Naranjos s/n, E-46022 Valencia, Spain. ³Ernst Ruska-Centre for Microscopy and Spectroscopy with Electrons ER-C, Forschungszentrum Jülich GmbH, D-52425 Jülich and Central Facility for Electron Microscopy GFE, RWTH Aachen University, 52074 Aachen, Germany. Correspondence and requests for materials should be addressed to M.E.I. (email: m.ivanova@fz-juelich.de) or J.M.S. (email: jmserra@itq.upv.es)

Although every specific application field sets particular requirements in terms of membrane stability, as a general rule, a good ceramic candidate has to remain phase and chemically stable at elevated temperatures in atmospheres possibly containing H_2 , H_2O , CO , CO_2 , CH_4 , SO_x , H_2S , and different levels of ash. Such atmospheres represent extreme operating environments for the majority of H_2 selective material classes, leading to material decomposition, membrane disintegration and performance degradation. Specifically, formation of undesired phases (carbonates, hydrates, sulfates) is critical for ceramic based membranes, while hydrogen-induced embrittlement and sulfur poisoning are particularly critical for Pd-based membranes^{7,11}.

Properties like high selectivity for H_2 , significant durability, mechanical and hydrothermal stability in reducing environments, as well as operating temperature ranges above 500 °C, make dense ceramic mixed proton-electronic conductors a promising alternative to precious metals and related alloys (Ag-Pd)¹², polymers¹³, metal-organic frameworks (MOFs)^{14,15}, zeolite¹⁶ or other ceramic microporous materials^{17,18}.

Apart from the stability issues which emerge to be solved, performance target for H_2 -flux of 1–2 mL_n·min⁻¹·cm⁻² at 600–700 °C has been set for H_2 -separation dense ceramic materials (based on the technical targets for dense metallic membranes for H_2 separation and purification). However, these values have not been yet achieved.

In the context of above, scientific community still faces the challenge of identifying highly performing and at the same time stable mixed proton-electronic conducting ceramic materials and to explore and utilize them as membranes in a number of chemical reactions and H_2 separation tasks at elevated temperatures.

In search for promising candidates for H_2 separation applications, electrical and proton transport properties of large number of oxide ceramics from several structural classes have been explored with particular intensity in the last years. Hence, a wide range of state-of-the art perovskite-based proton conductors^{19,20} to materials with less trivial structures and relatively novel to H_2 extraction application, as defective fluorites^{21–26}, pyrochlores²⁷, fergusonites^{28–32} has been covered. A comprehensive review on the electrical properties of a number of proton conductors could be found in ref. 33, while Table 1 presents a comparison of thickness-normalized H_2 permeation flux values from literature. As it could be inferred from the table, H_2 -permeation rates still remain lower than the milestone value at the target temperature.

The largest number of studies is however dedicated to the perovskite-based oxide ceramic materials, in particular with large lattice constant of the type $SrCeO_3$, $BaCeO_3$ and $BaZrO_3$ (Table 1). Substituted $BaCeO_3$ exhibits the highest levels of proton thermodynamic stability in the crystal structure remaining fully hydrated up to temperatures of about 600 °C but it is unstable in acidic gas environments due to its alkaline character^{19,66–68}.

Apart from their good proton conduction, perovskite-based materials e.g. of the type $BaCe_{1-x}M_xO_{3-\delta}$ exhibit also electronic conduction upon doping/substitution with M-cations with mixed valence^{40,42,69}. However, the levels of electronic conduction are significantly low relative to the ionic conduction. Indeed, a raise in the level of electronic conductivity can be pursued by adding a second electronically conducting crystalline phase to the pristine proton conductor. As reported by Elangovan *et al.*⁶¹, a successful approach to obtain H_2 -permeating material with high performance, is to combine (i) a protonic conducting perovskite phase $BaCe_{1-x}M_xO_{3-\delta}$ and (ii) an electronic conducting fluorite phase $Ce_{1-y}M_yO_{2-\delta}$ (M is metal dopant) into the so called *dual-phase ceramic material*, which at the end possesses increased ambipolar conductivity. The two crystalline phases form the *cer-cer composite* with certain degree of percolation, which provides efficient pathways for proton and electronic transport across the membrane. They are furthermore in a close contact at high temperature and reducing environments, therefore sufficient chemical and thermal compatibility between them is required. Elangovan *et al.*⁶¹, Ricote *et al.*⁷⁰, Medvedev *et al.*⁷¹ and Rebollo *et al.*⁶³ have shown the chemical compatibility and stability of systems consisting of $BaCe_{1-x}Ln_xO_{3-\delta}$: $Ce_{1-x}Ln_xO_{2-\delta}$ ($x = 0.1–0.2$) and $BaCe_{0.65}Zr_{0.2}Y_{0.15}O_{3-\delta}$: $Ce_{0.85}Ln_{0.15}O_{2-\delta}$ ($Ln = Y, Gd$), while Huang *et al.*⁷² reported the appearance of minor additional phase in the grain boundaries when Zr is doped in the perovskite phase. Furthermore, the addition of the doped ceria phase would enhance the stability of otherwise easily attacked by CO_2 and H_2O -containing environments $BaCeO_3$ phase due to a shift in thermodynamic equilibrium towards the reactant side⁷³. This leads to overall suppression of $BaCeO_3$ decomposition to $BaCO_3$, $Ba(OH)_2$ and CeO_2 .

In the present work composite ceramic membrane material with nominal composition $BaCe_{0.8}Eu_{0.2}O_{3-\delta}$: $Ce_{0.8}Y_{0.2}O_{2-\delta}$ (labeled BCEO:CYO) at 50:50 vol.% ratio was explored as H_2 permeation membrane in the temperature range 600–700 °C. This ratio was selected to ensure the largest degree of interaction between the two phases and sufficient transport pathways both for protons and electrons. In the context of above, acceptor substitution with 20 mol. % Eu^{3+} in $BaCeO_3$ and the same amount of Y^{3+} in CeO_2 was undertaken as a strategy to pursue an improvement and fine-tuning of transport properties of the composite ceramic material.

For the selection of the two substituents several factors were accounted. $BaCeO_3$ doped by Gd from rare earths (RE) in addition to Y, exhibits the highest ionic (protonic) conductivity among solid solutions $BaCe_{1-x}RE_xO_{3-\delta}$ ^{74–76}. Eu^{3+} ($4f^6$) and Gd^{3+} ($4f^7$) have the same valence state, nearly the same ionic radii and good geometrical compatibility with Ce as B-site ion in Ba-cerate. The ionic radius increases in the row $Gd \rightarrow Eu \rightarrow Sm$ and decreased protonic conductivity has been found for Sm due to the increased lattice distortion. However, similar lattice distortions and conductivities are expected to be produced by Eu^{3+} and Gd^{3+} in $BaCeO_3$. As demonstrated elsewhere⁷⁷, slightly higher values of the total conductivity in H_2 environments were determined for $BaCe_{0.85}Gd_{0.15}O_{3-\delta}$ in comparison with $BaCe_{0.85}Eu_{0.15}O_{3-\delta}$. Furthermore, there was practically no difference in conductivities under H_2/N_2 and air atmospheres measured for $BaCe_{0.85}Eu_{0.15}O_{3-\delta}$, while for $BaCe_{0.85}Tb_{0.15}O_{3-\delta}$ largely higher values were recorded under reducing environments. According to Radojkovic⁷⁸, Eu^{3+} substitution in $BaCeO_3$ leads to clear advantages over that with Y^{3+} or Gd^{3+} reported as the best proton conductors. One may highlight (i) the lower sintering temperature (reported to be below 1500 °C); (ii) the larger conductivity under wet H_2 conditions ($1.21 \cdot 10^{-2}$ S·cm⁻¹ at 600 °C) due to the larger unit cell volume and lattice distortion favoring intra-octahedral proton migration of lower activation energy; (iii) improved grain boundary conductivity ascribed to a decrease

Material	Ref.	Gas atmosphere Feed – Sweep	T (°C)	$j_{H_2, norm}$ (mL·min ⁻¹ ·cm ⁻¹)
<i>Defective fluorite structured materials</i>				
La _{5.5} WO _{11.25-δ}	25	wet 50% H ₂ in He – wet Ar	750/900	1.5·10 ⁻³ /4.7·10 ⁻³
La _{5.5} W _{0.8} Mo _{0.2} O _{11.25-δ}	25	wet 50% H ₂ in He – wet Ar	700	2.7·10 ⁻³
La _{5.5} W _{0.8} Re _{0.2} O _{11.25-δ}	25	wet 50% H ₂ in He – wet Ar	700	5.9·10 ⁻³
Nd _{5.5} WO _{11.25-δ}	34	wet 20% H ₂ in He – wet Ar	1000	1.2·10 ⁻³
(Nd _{5/6} La _{1/6}) _{5.5} WO _{12-δ}	35	wet 50% H ₂ in He – wet Ar	900	1.2·10 ⁻³
(La _{5/6} Nd _{1/6}) _{5.5} WO _{12-δ}	36	wet 50% H ₂ in He – wet Ar	900	1.4·10 ⁻³
Nd _{5.5} W _{0.5} Mo _{0.5} O _{11.25-δ}	37	wet 50% H ₂ in He – wet Ar	900	7.5·10 ⁻³
Nd _{5.5} W _{0.5} Re _{0.5} O _{11.25-δ}	38	wet 50% H ₂ in He – wet Ar	900	4.1·10 ⁻³
<i>Perovskite structured materials</i>				
BaCe _{0.80} Y _{0.10} Ru _{0.10} O _{3-δ}	39	wet H ₂ in Ar – Ar	800	4.3·10 ⁻³
BaCe _{0.95} Nd _{0.05} O _{3-δ}	40	wet 80% H ₂ in He – dry Ar + Ne	900	1.3·10 ⁻³
BaZr _{0.80} Y _{0.15} Mn _{0.05} O _{3-δ}	41	wet 50% H ₂ in He – wet Ar	900	1.4·10 ⁻³
SrCe _{0.95} Tm _{0.05} O _{3-δ}	42	10% H ₂ in He – air	700/900	1.2·10 ⁻³ /1.9·10 ⁻³
SrCe _{0.95} Tm _{0.05} O _{3-δ}	43	10% H ₂ in He – air	700/900	2.6·10 ⁻³ /6.4·10 ⁻³
SrCe _{0.95} Tm _{0.05} O _{3-δ}	44	10% H ₂ dry in He – 20% O ₂ in Ar	750/900	4.3·10 ⁻³ /6.8·10 ⁻³
SrCe _{0.95} Tb _{0.05} O _{3-δ}	45	20% H ₂ in He – CO in Ar	750/900	4.0·10 ⁻⁴ /1.6·10 ⁻³
SrCe _{0.95} Y _{0.05} O _{3-δ}	46	80% H ₂ in He – Ar	900	3.2·10 ⁻⁴
SrCe _{0.95} Yb _{0.05} O _{3-δ}	47	10% H ₂ in He – air	677	2.7·10 ⁻³
SrCe _{0.95} Eu _{0.05} O _{3-δ}	48	100% H ₂ – He	700/850	2.3·10 ⁻⁴ /7.4·10 ⁻⁴
SrCe _{0.95} Sm _{0.05} O _{3-δ}	48	100% H ₂ – He	850	5.4·10 ⁻⁴
SrCe _{0.75} Zr _{0.20} Tm _{0.05} O _{3-δ}	49	H ₂ in He – wet Ar	900	5.0·10 ⁻³
SrCe _{0.75} Zr _{0.20} Tm _{0.05} O _{3-δ}	44	10% H ₂ dry in He – 20% O ₂ in Ar	750/900	8.0·10 ⁻⁴ /2.4·10 ⁻³
SrCe _{0.70} Zr _{0.25} Ln _{0.05} O _{3-δ} (Ln = Tm, Yb)	50	wet 20% H ₂ – wet sweep (not specified)	900	2.3·10 ⁻⁴
SrCe _{0.65} Zr _{0.20} Eu _{0.15} O _{3-δ}	51	100% H ₂ – He	900	8.5·10 ⁻⁴
SrZr _{0.95} Y _{0.05} O _{3-δ}	47	20% H ₂ – air in He	700	<2.3·10 ⁻⁵
<i>Cer-Met dual phase materials</i>				
BaCe _{0.95} Tb _{0.05} O _{3-δ} :Ni (50:50 wt.%)	52	50% H ₂ in N ₂ – He	850	8.3·10 ⁻³
BaCe _{0.90} Y _{0.10} O _{3-δ} :Ni (60:40 vol.%)	53	4% H ₂ in He – 100 ppm H ₂ in N ₂	800	1.7·10 ⁻²
BaCe _{0.80} Y _{0.20} O _{3-δ} :Ni (60:40 vol.%)	54	3.8% H ₂ in N ₂ – 100 ppm H ₂ in N ₂	900	2.0·10 ⁻³
BaCe _{0.85} Zr _{0.10} Tb _{0.05} O _{3-δ} :Ni (50:50 wt.%)	55	50% H ₂ in 50% He – Ar	800	8.5·10 ⁻³
BaCe _{0.70} Zr _{0.10} Y _{0.20} O _{3-δ} :Ni (60:40 vol.%)	56	4% H ₂ in He – 100 ppm H ₂ in N ₂	900	5.6·10 ⁻³
BaCe _{0.70} Zr _{0.10} Y _{0.10} Yb _{0.10} O _{3-δ} :Ni (60:40 vol.%)	57	20% H ₂ wet, 60% CO ₂ , 20% He – N ₂	900	3.5·10 ⁻³
Ce _{0.50} La _{0.4875} Ca _{0.0125} O _{2-δ} :Ni (60:40 vol.%)	58	wet 20% H ₂ , 77% N ₂ – Ar	900	1.5·10 ⁻³
YSZ:Pd (40:60 vol.%)	59	90% H ₂ in He – N ₂	400/900	4.7·10 ⁻² /9.4·10 ⁻²
<i>Cer-Cer dual phase materials</i>				
La _{5.5} WO _{11.25-δ} :La _{0.87} Sr _{0.13} CrO _{3-δ} (50:50 vol.%)	60	wet 50% H ₂ in He – wet Ar	700	5.5·10 ⁻³
BaCe _{0.80} Eu _{0.20} O _{3-δ} :Ce _{0.80} Eu _{0.20} O _{2-δ} (50:50 vol.%)	61	H ₂ , CH ₄ , H ₂ O, CO, CO ₂ – He	900	<7.0·10 ⁻²
BaCe _{0.80} Y _{0.20} O _{3-δ} :Ce _{0.80} Y _{0.20} O _{2-δ} (50:50 wt.%)	62	wet 50% H ₂ in He – wet Ar	900	1.1·10 ⁻²
BaCe _{0.65} Zr _{0.20} Y _{0.15} O _{3-δ} :Ce _{0.85} Gd _{0.15} O _{2-δ} (50:50 vol.%)	63	wet 50% H ₂ in He – wet Ar	755	1.76·10 ⁻²
BaCe _{0.20} Zr _{0.70} Y _{0.10} O _{3-δ} :Sr _{0.95} Ti _{0.90} Ni _{0.10} O _{3-δ} (50:50 vol.%)	64	9% H ₂ in He – dry Ar	800	1.1·10 ⁻³
SrZrO ₃ :SrFeO ₃ (80:20 vol.%)	65	H ₂ in He – wet Ar	900	4.8·10 ⁻³

Table 1. Based on literature summary of thickness (L_{mem})-normalized values of H₂ permeation rates $j_{H_2, norm}$ through ceramic membranes.

in band gap energy related to the transition between O 2p valence band to Ce 4f conduction band; and (iv) dominating proton conductivity under OCV conditions at 650 °C and 700 °C.

On the other hand, in reducing atmospheres, Y-substituted CeO₂ exhibits predominantly electronic conduction via small polaron hopping mechanism due to Ce^{4+/3+} variable valence. Besides, detailed structural and phase characterization via Rietveld refinement on XRD will help to evaluate the phase formation and phase stability of the cer-cer composite supported by microstructural study via SEM and HR-TEM. Electrical conductivity properties of the composite material and its constituting phases were studied to elucidate the relative contributions of each phase in the composite. In addition, hydrogen permeation of the composite membrane with thickness of 500 μm was characterized as a function of the temperature, the hydration conditions and the hydrogen concentration in the feed. Membrane stability in CO₂-containing atmospheres was studied *in situ* with H₂ permeation measurements to conclude on eventual phase, microstructural and performance degradation effects.

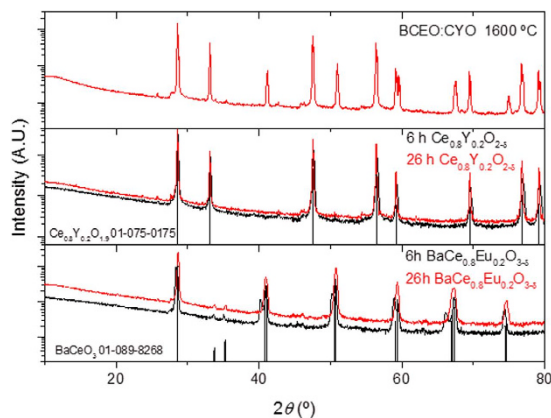


Figure 1. XRD diffraction patterns of BCEO (bottom); CYO (middle) synthesized by solid-state reaction at 1400 °C for 6 and 26 h; and the BCEO:CYO (top) composite pattern sintered for 10 h at 1600 °C.

Results and Discussion

Structural and phase composition study. Figure 1 shows the XRD patterns of BCEO and CYO synthesized via the conventional solid-state route at 1400 °C, and the composite pattern resulting from mixing them in a 50:50 vol.% ratio and sinter for 10 h at 1600 °C. Rietveld refinement on the XRD performed on the BCEO and CYO separately showed that the single phases were not formed after 6 h of calcination. XRD patterns revealed a mixture of tetragonal and orthorhombic perovskite phases for BCEO and two fluorite phases with different Y content (details are summarized in the Table 2). An extra thermal treatment of 20 h (in total 26 h) allows single phase samples with sharp defined peaks to be obtained. Besides, once the pressed pellet is sintered at 1600 °C, the observed splitting of peaks disappear and XRD reveals that a single BCEO perovskite phase and a single CYO fluorite were formed. The presence of other oxides was not observed.

As it can be observed from Table 2, the lattice parameters of the two phases constituting the dual phase ceramics disclosed certain deviation from the nominal stoichiometry. The ceria phase shows a cubic fluorite structure with a lattice parameter of 5.411 (1) Å, clearly shifted from the theoretical value of 5.405 Å estimated by Kim's empirical formula⁷⁹ for 20 mol.% yttria substitution in CeO₂ (and from the 5.405 Å obtained experimentally for the single doped ceria phase). The calculation took into account the ionic radii in 8-fold coordinated Ce⁴⁺ and Y³⁺ cations, which are 0.97 and 1.019 Å, respectively. Since the ionic radii of Eu³⁺ is 1.066 Å, the substitution of Ce⁴⁺ cations by Eu³⁺ is suggested. By using the experimental cell parameter obtained for the fluorite phase, Kim's formula can be reversely used to estimate to which extent Eu migrated to the ceria phase. As there are not yttrium related impurities, the yttrium content in the fluorite was fixed to 20 mol.%, which gives a value of $x = 10.5$ mol.% for Eu³⁺ and corresponds to stoichiometry Ce_{0.695}Y_{0.2}Eu_{0.105}O_{2.6}. This value indicates that practically all the Eu introduced by the perovskite phase has migrated to the fluorite phase. The mass balance by ICP-OES (Supplementary information, Table S1) indicates that the barium was not deficient after the sintering (see Experimental Section, Sample preparation paragraph). The unit cell volumes of pure BaCeO₃, BaCe_{0.9}Eu_{0.1}O_{2.95} according to⁷⁸, BaCe_{0.8}Eu_{0.2}O_{2.9} after 26 h at 1400 °C and for Ba-cerate phase in the composite material BaCe_{0.8}Eu_{0.2}O_{2.9}:Ce_{0.8}Y_{0.2}O_{1.9} after 10 h at 1600 °C are respectively: 340 Å³, 341.79 Å³, 342.4 Å³ and 340.73 Å³, showing that (i) with increasing the Eu amount the volume expands as expected; and (ii) Ba-cerate in the composite is practically Eu-depleted.

Microstructural characterization. FE-SEM analysis of the polished cross-section of the BCEO:CYO membrane revealed a high relative density (>98%), although some occluded porosity is still present (Fig. 2a–f). The thermal expansion coefficient (TEC) of the composite material in air ($12.4 \cdot 10^{-6} \text{ K}^{-1}$) shows identical behavior during heating and cooling cycles in air (Supplementary information, Figure S2). No cracks related to the TEC thermochemical cycles were detected due to the good thermal compatibility of the two ceramic components. BSE-SEM (Fig. 2c–e) and EDS analysis (Fig. 2f) show dark grains corresponding to the CYO phase, as well as a bright phase corresponding to BCEO. In addition, Fig. 2c,f shows the EDS linescan analysis of a fracture cross-section of the membrane and the corresponding Ba and Y concentration profiles. Neither Ba (in Fig. 2f the blue line) nor Y (in Fig. 2f the red line) interdiffusion between both phases occurs. The topography and distinct textures observed in the polished cross-section for each phase originates from the difference in hardness, i.e., the dark phase (CeO₂) is harder, and this effect was previously reported for BaCeO₃:CeO₂ composites⁷⁰.

Further detailed insight in composite microstructure was achieved by the TEM and high resolution scanning transmission electron microscope with high-angle annular dark-field imaging (HRSTEM-HAADF) (Fig. 3). A low-magnification TEM image acquired from the composite sample as-sintered at 1600 °C is shown in Fig. 3a (Composite sample, nominally labeled BCEO:CYO, was actually named BaCeO:CeYEuO in the TEM image after its actual composition with Eu predominantly located in the CYO phase). The sample is composed of randomly oriented, well-connected and packed grains with sizes ranging from 0.5 μm to 2 μm. The grains have a polygonal shape, which minimizes their surface energy. Two types of grains were observed: some grain's interiors were decorated with dotty/fuzzy contrast, while other grains surface was even. Furthermore, dotty contrast inside grains is sensitive to the grains relative orientation with respect to the electron beam. The slight tilt of the grain

Nominal starting compounds	Phase composition	Space group	Lattice parameter(s), (Å)	Phase wt. %	Phase D_{th} (g/cm ³)	Rwp, %
BaCe _{0.8} Eu _{0.2} O _{2.9} 1400 °C/6h	BaCe _{0.8} Eu _{0.2} O _{2.9} tetragonal	P-42m	a = 4.388 (1) c = 4.465 (1)	86	6.30	6.7
	BaCe _{0.8} Eu _{0.2} O _{2.9} orthorhombic	Pmcn	a = 6.245 (1) b = 8.770 (1) c = 6.272 (1)	14	6.31	
BaCe _{0.8} Eu _{0.2} O _{2.9} 1400 °C/26h	BaCe _{0.8} Eu _{0.2} O _{2.9} orthorhombic	Pmcn	a = 6.229 b = 8.782 c = 6.257 (1)	100	6.35	6.6
Ce _{0.8} Y _{0.2} O _{1.9} 1400 °C/6h	Ce _{0.9} Y _{0.1} O _{1.95} cubic	Fm-3m	a = 5.411(1)	45	6.93	5.3
	Ce _{0.8} Y _{0.2} O _{1.9} cubic	Fm-3m	a = 5.401(1)	55	6.75	
Ce _{0.8} Y _{0.2} O _{1.9} 1400 °C/26h	Ce _{0.8} Y _{0.2} O _{1.9} cubic	Fm-3m	a = 5.405(1)	100	6.8	5.9
BaCe _{0.8} Eu _{0.2} O _{2.9} ; Ce _{0.8} Y _{0.2} O _{1.9} 1600 °C/10h	BaCe _{1-x} Eu _x O _{3-δ} orthorhombic	Pmcn	a = 8.786(1) b = 6.245(1) c = 6.210(1)	46	6.34	5.4
	Ce _{0.695} Y _{0.2} Eu _{0.105} O _{2.8} cubic	Fm-3m	a = 5.411(1)	54	6.77	

Table 2. Rietveld refinement results from the XRD patterns of BCEO and CYO synthesized via the conventional solid-state route at 1400 °C during 6 h and 20 h (in total 26 h), and of BCEO:CYO dual-phase pellet (50:50 vol.%) sintered at 1600 °C for 10 h. For reference, the lattice parameters of pure BaCeO₃ are a = 8.776(1) Å, b = 6.234(1) Å, c = 6.214(1) Å.

could enhance or diminish the dotted contrast significantly (Fig. 3b,c). HR-TEM investigation does not reveal any interface phases at the grain boundaries (not shown). STEM-HAADF images acquired using strong elemental contrast (Z-contrast) conditions are shown in Fig. 3d. The dotted/fuzzy contrast is evidenced under such imaging conditions as well. EDX analysis (Fig. 3d,e) revealed that dotted/fuzzy contrast rich grains are composed of Ce, Y, Eu and O elements, while other grains consist of Ba, Ce and O. The dotted pattern contrast might be attributed to Eu presence in CYO grains, which is associated with high point-defect density caused by incorporation of Eu into this phase. Furthermore, no migration of Y from the fluorite to the perovskite could be evidenced (Fig. 3(e)). HR-STEM-HAADF images recorded from the two grain types in range of crystallographic projections exhibit single crystal structure as shown in Fig. 3f. Dotted contrast is absent in HRSTEM-HAADF imaged for CYO (Ce-Y-Eu-O) grain due to channeling contrast mechanisms dominant at those imaging conditions. By correlating selected area electron diffraction (SAED) and HRSTEM-HAADF images with crystal structure data, the CYO (actually CYEuO) grains showed Fm-3m space group, while BCEO (actually BCO) grains exhibit Pmcn space group crystal structure, both in agreement with the Rietveld refinement made on the XRD patterns. As a summary, the microstructural analysis confirms that Eu diffused from the BCEO perovskite to the CYO fluorite when exposed to high temperature, as previously shown in the XRD section with no evidence for Y diffusion from the fluorite to the perovskite.

Since the composition and microstructure of both phases is pure, without grain boundary segregations electrical and electrochemical study was performed in order to evaluate the transport properties of this dual-phase material.

Electrochemical characterization. Figure 4 displays the total conductivity corresponding to the single phase materials BaCe_{0.8}Eu_{0.2}O_{3-δ} (BCEO) and Ce_{0.8}Y_{0.2}O_{2-δ} (CYO), and the composite material BCEO:CYO with nominal composition BaCe_{0.8}Eu_{0.2}O_{3-δ}:Ce_{0.8}Y_{0.2}O_{2-δ}. The samples have been measured as a function of inverse temperature under H₂, H₂+H₂O, D₂ and D₂+D₂O atmospheres. Within the studied range of temperatures (from 800 °C to 400 °C), BCEO exhibits mainly protonic conductivity, ascertained from the H/D isotopic and hydration effect, i.e. lower conductivity in D₂ than in H₂ atmospheres and higher conductivity in wet than in dry atmospheres. Above 750 °C, the different conductivity curves converge due to the progressive oxide dehydration with temperature, leading to significant drop in proton concentration. On the other hand, CYO possesses higher conductivity in dry atmospheres than in wet conditions (wet atmospheres signify less reducing conditions than dry atmospheres) suggesting that electronic transport prevails under these conditions. Finally, BCEO:CYO composite shows prevailing *n*-type conduction behaviour and conductivity values similar to CYO, indicating proper percolation of this electron conducting component, as previously suggested by the SEM analysis.

In order to disclose the predominant transport of these compounds, *p*O₂ effect on the conductivity was also studied under wet reducing conditions (Fig. 5). The BCEO behavior as a prevailing proton conductor deduced from the observed H/D isotopic effect is confirmed by the relationship $\sigma \propto pO_2^0$ in all studied temperatures i.e., the conductivity is independent on the *p*O₂ values. On the other hand, CYO exhibits predominant *n*-type electronic conduction following a power law of $\sigma \propto pO_2^{-1/4}$ as it has been reported previously for CYO material^{80,81}. Finally, from the relationship $\sigma \propto pO_2^{-1/6}$ observed for the composite BCEO:CYO, it can be assumed an intermediate behaviour, i.e. it is mainly *n*-type electronic conductor but presents a significant ionic contribution, arising from the physical mixture of the two different conductors.

Temperature programmed reduction (TPR) measurements (Figure S3 in Supplementary Information) were performed in order to study the redox behavior of the single compounds and the composite, and to correlate with the conductivity data. The CYO sample shows the maximum of its reduction peak at 725 °C, ascribed to the reducible bulk Ce⁴⁺. This reduction temperature agrees with previous studies on doped CeO₂⁸². Regarding BCEO, a broad reduction peak is observed between 300–700 °C, which can be attributed to the Ce⁴⁺ reduction and some oxygen release. The reduction of Eu³⁺ to Eu²⁺ is not expected in the considered temperature range as it was observed previously for Eu doped NdWO compound⁸³. Finally, the Ce⁴⁺ reduction in the sintered BCEO:CYO samples is shifted to higher temperatures presenting its maximum at 800 °C. The lower reducibility of Ce⁴⁺ in this

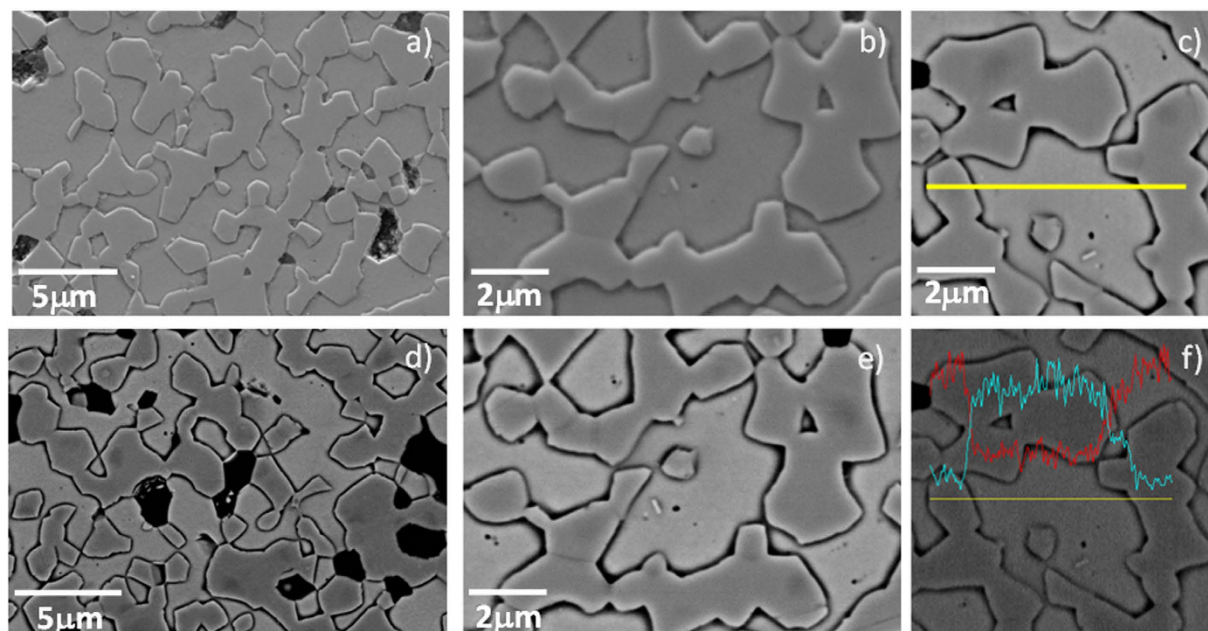


Figure 2. (a,b) SEM, (c–e) BSE-SEM and (f) EDS linescan analysis of the fractured cross-section of the BCEO:CYO membrane sintered at 1600 °C.

sample could be ascribed to the different stoichiometry of the BCEO and doped ceria grains as compared with the separate single material, as this is previously stated for instance in heavily doped cerias⁸⁴.

Hydrogen permeation measurements. Permeation properties were thoroughly studied by analyzing the influence of the environment humidification and temperature on the H₂ permeation. Three different configurations, depicted in Fig. 6a, were selected in order to study the effect of humidification: (A) only feed side humidified, (B) both membrane sides humidified and (C) only sweep side humidified. 50 vol.% H₂ in He was employed as feed gas and Ar was used as sweep gas. Figure 6b plots the H₂ permeation behavior through the composite membrane as a function of the temperature in the three configurations. When only the feed side is humidified (configuration A), H₂ flow is below 0.05 mL·min⁻¹·cm⁻² due to the low concentration of protons as a result of the large pH₂O gradient across the membrane. When both sides are humidified (configuration B), the obtained H₂ flow is one order of magnitude higher than in configuration A (0.4 mL·min⁻¹·cm⁻² at 700 °C). This important increase is attributed to the faster proton transport through the membrane, as a consequence of the higher hydration of the material and hence the higher concentration of protonic defects⁶³. In addition to proton transport, H₂ is also generated at the sweep side by water splitting reaction mediated by the oxygen ion diffusion from the high pO₂ side (Ar sweep) to the lower pO₂ side (H₂ feed). The oxygen transport takes place preferentially through the CYO phase, since this phase presents significant oxygen ion conductivity at elevated temperatures⁸⁰, although it is still one order of magnitude lower than the electronic conductivity in reducing conditions. Finally, for humidified sweep gas (configuration C), the H₂ flow increases further, reaching values of 0.61 mL·min⁻¹·cm⁻² at 700 °C. This increase in H₂ production stems from the higher magnitude of water splitting process since a higher pO₂ gradient is imposed across the membrane as compared to configuration B.

H₂ permeation was also studied as a function of the hydrogen concentration (pH₂) in the feed side (Fig. 6c,d). Irrespective of the humidification conditions, H₂ flow rises with increasing pH₂ as it is postulated by the Wagner equation, which describes the transport of both protons and oxygen ions. Furthermore, H₂ permeation was investigated by using lower pH₂O at the sweep side, pH₂O = 0.0094 atm instead of 0.042 atm. Results are shown in Fig. 7a–c. H₂ flows obtained at 700 °C sweeping pH₂O = 0.042 atm are 19% and 8% higher than the values obtained for pH₂O = 0.0094 atm, in configurations B and C, respectively (Fig. 7a). Assuming that the partial conductivities are constant in the studied pO₂ and pH₂O ranges, and that H₂ transport can be described by Wagner's, the H₂ flow could be expressed as it is indicated in eq. 1, where the first term corresponds to the H₂ permeating through the membrane and the second one responds to the H₂ produced by water splitting.

$$J_{H_2} \approx \frac{RT}{4F^2L} \frac{(\sigma_{H^+} \cdot \sigma_{e^-})}{\sigma_T} \ln \frac{p(H_2, feed)}{p(H_2, perm)} + \frac{RT}{8F^2L} \frac{(\sigma_{O^{2-}} \cdot \sigma_{e^-})}{\sigma_T} \ln \frac{p(O_2, perm)}{p(O_2, feed)} \quad (1)$$

With pH₂O = 0.042 atm, $\ln \frac{p(O_2, perm)}{p(O_2, feed)}$ is 1.285 and 1.121 times higher than the corresponding to pH₂O = 0.0094 atm in configuration B and C, respectively. On the other hand, the variation in the term $\ln \frac{p(H_2, feed)}{p(H_2, perm)}$ by changing the pH₂O is almost negligible. From these results, it could be concluded that an

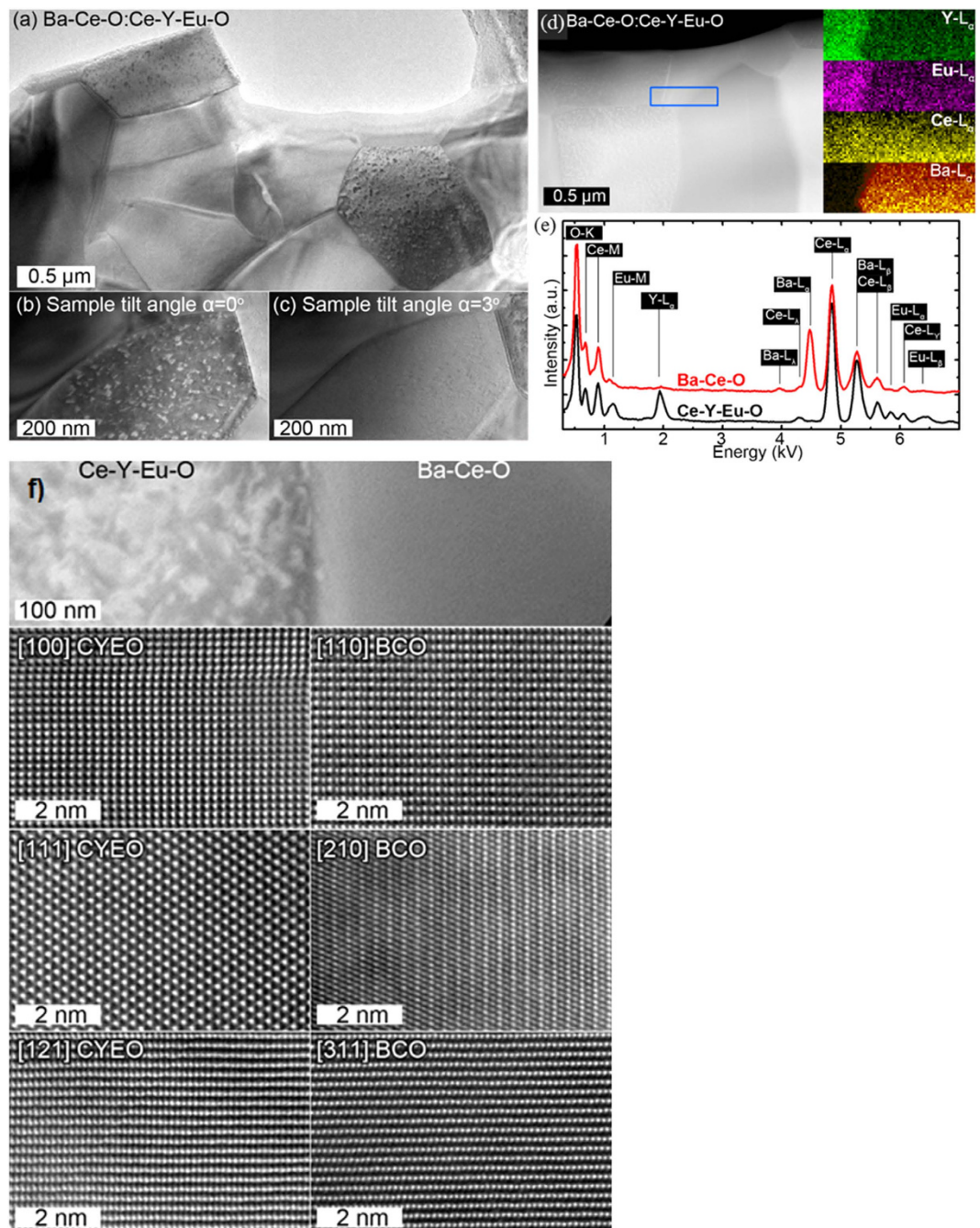


Figure 3. (a) Overview TEM image acquired from BCEO:CYO sample sintered at 1600 °C for 10 h; (b)-(c) shows the grain contrast dependence with distinct sample orientation (tilt); (d) Overview STEM-HAADF acquired from BCEO:CYO samples together with corresponding elemental EDX areal maps; (e) integrated EDX spectrum from the CYO and BCEO grains; and (f) High-resolution STEM-HAADF images acquired from CYO (Ce-Y-Eu-O) grain (left column) and BCEO (Ba-Ce-O) grain (right column) in the BCEO:CYO dual phase sample utilizing different crystallographic projections.

important contribution to the H_2 flow observed comes from the water splitting and the changes observed when p_{H_2O} decreases are mainly ascribed to the reduction of the oxygen transport through the membrane.

Step-changes from configurations C to A were monitored for both conditions (Fig. 7b,c). Hydrogen fluxes decrease changing from configuration C to B and A for $p_{H_2O} = 0.042$ atm (Fig. 7b) and they increase changing from configuration A to B and C for $p_{H_2O} = 0.0094$ atm (Fig. 7c). The quick response for both conditions is mainly related to the important changes in H_2 production by water splitting¹¹.

In the light of the previous reports on similar cerceer composites^{63,64,85}, the effect of Pt layer applied on the surface of the tested membrane on water splitting reaction must be also taken into consideration. According to⁶², no contribution of water splitting to the H_2 permeation could be evidenced at lower water vapor pressure at the

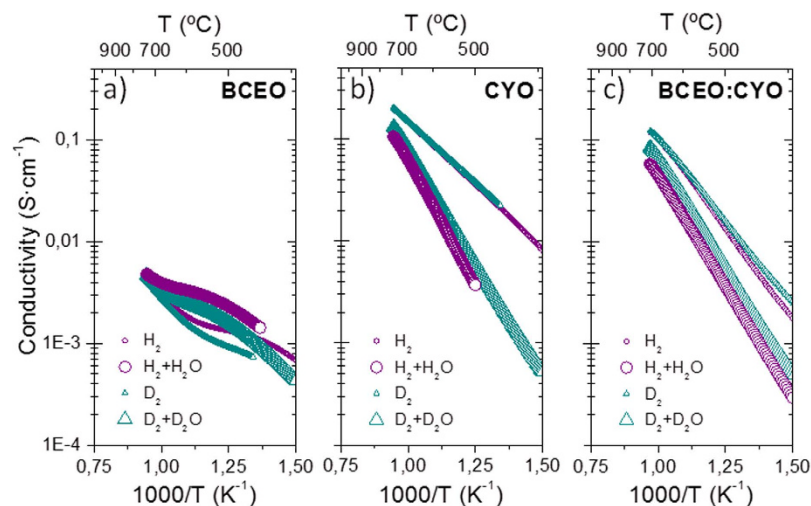


Figure 4. Total conductivity as a function of inverse temperature measured under four different reducing atmospheres: 5 vol.% H₂ in He and 5 vol.% D₂ in He both dry and moist (H₂ and D₂ humidified with H₂O and D₂O at room temperature, respectively) for (a) BCEO, (b) CYO and (c) BCEO:CYO composite.

sweep side due to omitting Pt catalyst layer. However, cerceer composites were just recently identified as promising candidates for H₂ permeation membranes, therefore detailed studies have not been yet done to assign different reaction contributions to the overall H₂ flux.

Stability tests. The assessment of the H₂ permeation stability under CO₂ atmospheres was carried out at 700 °C during 6 days by using 15 vol.% CO₂ in Ar as sweep gas, 50 vol.% H₂ in He as feed gas and humidifying both sides of the membrane (configuration B). Figure 8a shows that the H₂ flow obtained under CO₂ containing atmosphere is significantly lower than that obtained by using pure Ar, around 0.15 mL·min⁻¹·cm⁻². This drop in the H₂ flux by using CO₂ could be ascribed to the CO₂/H₂ and/or CO₂/O₂ competitive adsorption on the membrane surface^{11,63} that slows down the gas exchange. Besides, the flux equilibration in these conditions takes more than 2 days.

TG analysis was performed under 5 vol.% CO₂ balanced with Ar by using crushed samples sintered at 1600 °C. Figure 8b indicates that CYO sample does not suffer any CO₂ uptake under CO₂ containing atmospheres within the studied temperature range. On the other hand, a mass gain is observed for BCEO sample above 500 °C, which is ascribed to the carbonation of the sample^{37,66,73}. However, the mass of the composite BCEO:CYO does not increase indicating that no carbonation process is taking place. It can be concluded that the addition of ceria to the cerate allows shifting the carbonation equilibrium and consequently improves the stability of the composite.

The structural stability of BCEO:CYO membrane after 13 days on stream (total duration of the permeation measurements, including CO₂ stability measurement) was verified by XRD (Fig. 9a) and FE-SEM (Fig. 9b–e) analysis. Figure 9a depicts the XRD patterns recorded on dual-phase BCEO:CYO sintered samples before permeation (labeled BP-1600/10 h) and after the H₂-permeation tests (labeled AP). Both the feed and sweep sides of the membrane were investigated to detect any phase changes or formation of carbonates (denoted with AP-F and AP-S for feed and sweep side of the membrane, respectively). As reference, the peak positions and related intensities for BaCeO₃ and Ce_{0.8}Y_{0.2}O_{1.9} are presented at the bottom of the figure. Up to the analytical limits of the XRD device, no changes in the structure were found and both fluorite and perovskite phases are well distinguished. The peaks marked by a diamond correspond to Pt traces from the catalytic layer. The XRD pattern of the sweep side of the membrane after permeation shows broader peaks, which could indicate some modification in the surface microstructure.

Figure 9b–e presents the FE-SEM (b), and the BSE-SEM (c,d) micrographs and EDS linescan (e) analysis of the membrane after the permeation measurements (note that the membrane is the same specimen for all the H₂ permeation measurements described in the work). Neither morphological nor structural changes were detected.

Finally, stability of dual phase composite material was checked after running the sintered membranes in continuous electrical tests for 670 h under 4% H₂-containing dry reducing conditions, including several cycling steps from room temperature up to 900 °C and 1000 °C with holding times at these temperatures of 48 h and 20 h, respectively. TEM investigation of a reference sample and of post-treatment specimens is shown in Figure S4 in Supplementary Information. No morphological differences between the reference and post-treatment membranes and no grain boundary segregations were detected resulting from the 670 h continuous operation under reducing conditions.

Conclusions

We have presented a dual phase material based on perovskite and fluorite exhibiting both high electronic and H⁺/O²⁻ co-ionic conductivity. Nominal BaCe_{0.8}Eu_{0.2}O_{3-δ} (BCEO) and Ce_{0.8}Y_{0.2}O_{2-δ} (CYO) were mixed in a 50:50 vol.% ratio. Eu³⁺ cations originally present in BCEO diffused to CYO during the sintering step (Ce_{0.695}Y_{0.2}Eu_{0.105}O_{2-δ};

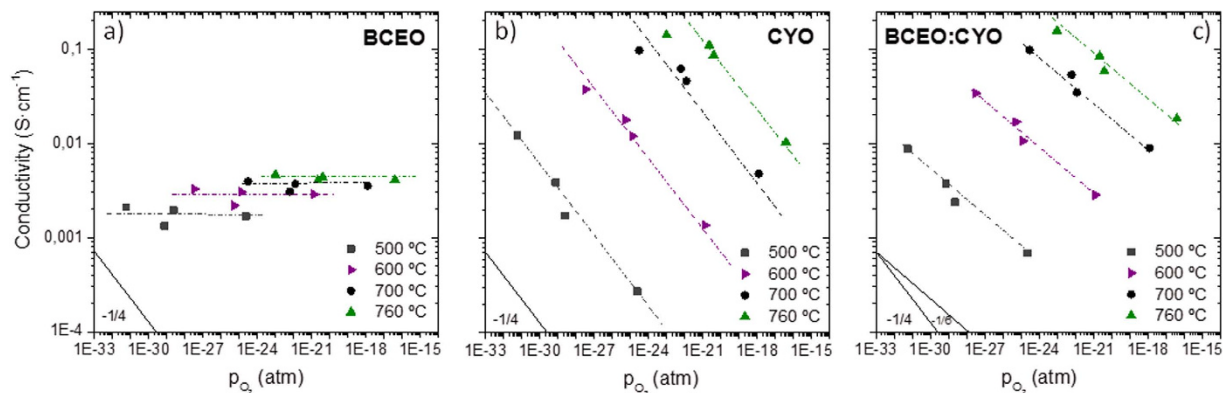


Figure 5. Total conductivity as a function of p_{O_2} under wet reducing atmospheres at four different temperatures for (a) BCEO, (b) CYO and (c) BCEO:CYO.

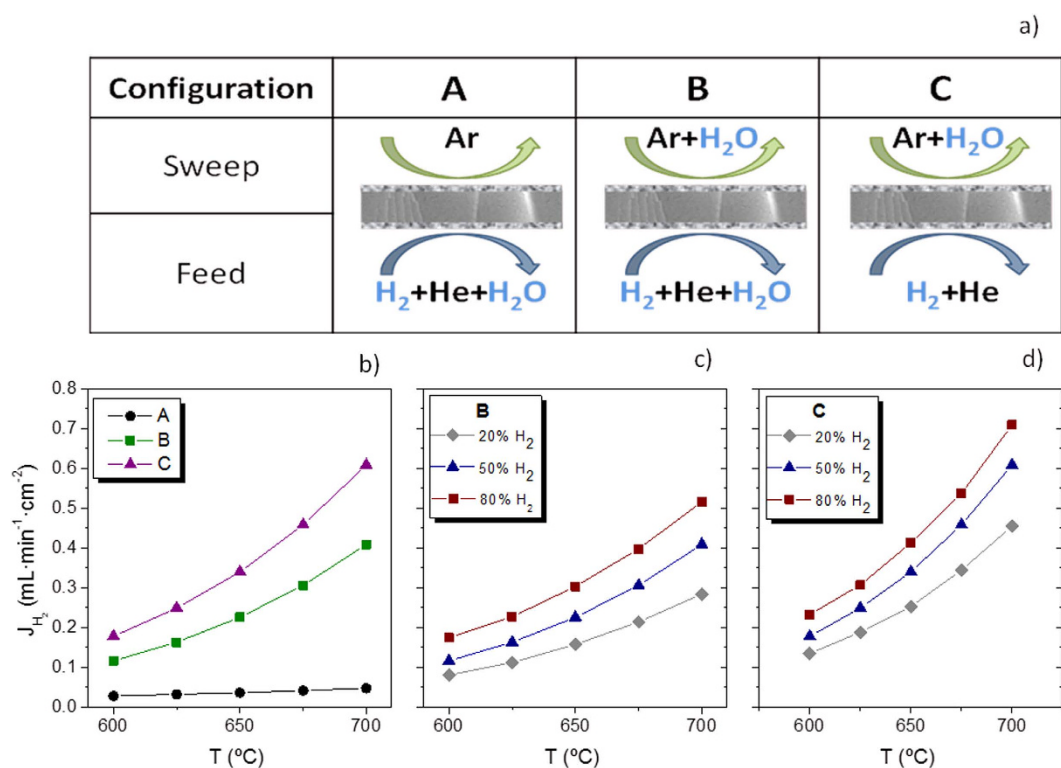


Figure 6. (a) Representation of configurations for membrane testing; (b) H_2 flow as a function of temperature in the three configurations A, B and C with different hydration degree, feed stream 50% H_2 in He; and (c,d) H_2 flow as a function of temperature for different p_{H_2} feeding in configuration B and C.

CYEuO) as revealed by TEM analysis. DC-conductivity using a deuterium tracer showed that the composite is mixed protonic-electronic conductor (MPEC). Indeed, BCEO behaves as a prevailing proton conductor and CYO (CYEuO) as a mixed oxygen ionic and electronic conductor.

H_2 permeation through a thick planar BCEO:CYO membrane was measured in different gas hydration configuration. The reached H_2 fluxes are among the highest reported for ceramic membranes up to date 0.4 and 0.61 mL·min⁻¹·cm⁻² at 700 °C under configuration B and C, respectively (or thickness-normalized values of 0.02 and 0.0305 mL·min⁻¹·cm⁻¹ at 700 °C under configuration B and C, respectively). This remarkably high permeability originates from the transport of protons as well as from the hydrogen generated by water splitting on the permeate side (the high oxygen partial pressure side) of the membrane due to the oxygen ion transport in ceria. The membrane material was stable after 670 h continuous operation under 4% H_2 -containing dry reducing conditions, as well as in 15% CO_2 containing atmosphere, although the resulting flux was lower than in pure Ar due to the competitive adsorption in the surface between H_2/O_2 and CO_2 . The stability in CO_2 is tentatively attributed to the protective effect of the ceria phase over the cerate phase.

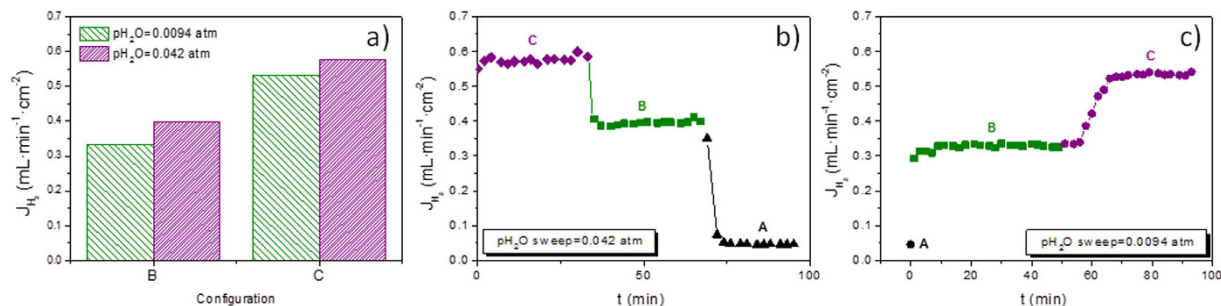


Figure 7. (a) H_2 flows obtained at 700 °C in configurations B and C for $p_{H_2O}(\text{sweep}) = 0.042$ atm and $p_{H_2O}(\text{sweep}) = 0.0094$ atm. (b,c) H_2 flow variation produced by the step-change from C to B to A with (b) $p_{H_2O}(\text{sweep}) = 0.042$ atm and (c) $p_{H_2O}(\text{sweep}) = 0.0094$ atm at 700 °C feeding 50 vol.% H_2 .

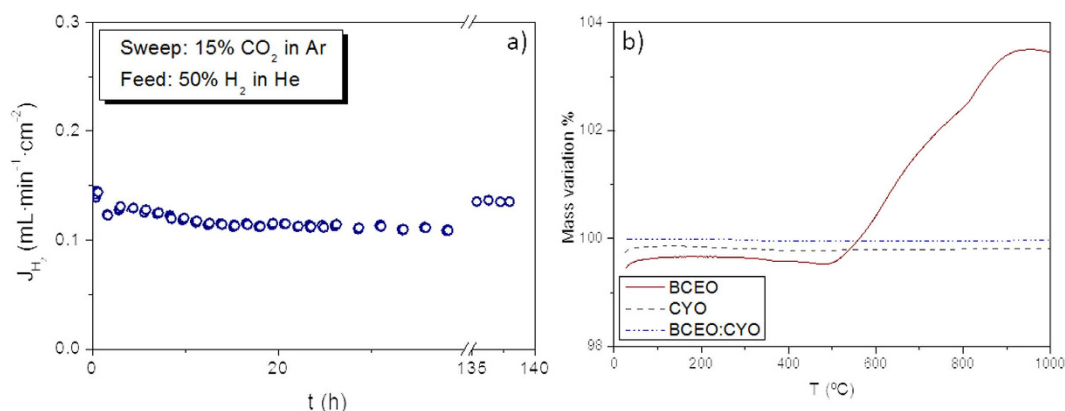


Figure 8. (a) H_2 flow as a function of time by using 15 vol.% CO_2 in Ar as sweep gas and 50 vol.% H_2 in He as feed gas at 700 °C. Both sides of the membrane were humidified (configuration B). (b) TG measurements of BCEO, CYO and BCEO:CYO under 5 vol.% CO_2 in Ar.

Experimental Section

Sample preparation. Materials with nominal composition $BaCe_{0.8}Eu_{0.2}O_{3-\delta}$ (BCEO) and $Ce_{0.8}Y_{0.2}O_{2-\delta}$ (CYO) were synthesized via the conventional solid-state route. Stoichiometric amounts of high-purity $BaCO_3$ and CeO_2 , Eu_2O_3 , Y_2O_3 (Sigma Aldrich) were weighted, mixed and ball-milled in ethanol. The solid-state synthesis for both compounds took place at 1400 °C for 6 h in air. A second calcination step (20 h) was required for the complete formation of the perovskite single phase, and resulting products were milled in ethanol. After drying, the two powder products were mixed in 50:50 vol.% ratio and were homogenized 24 h in ethanol, dried and sieved. Uniaxially pressed samples were sintered at 1600 °C for 10 h leading to formation of dual phase BCEO:CYO material with nominal stoichiometry $BaCe_{0.8}Eu_{0.2}O_{3-\delta};Ce_{0.8}Y_{0.2}O_{2-\delta}$. Samples were grinded to remove the defective top layer and no Ba-deficiency or secondary oxide exclusions compensating eventual Ba evaporation were detected by ICP-OES. Relative density of more than 98% was determined via the Archimedes approach on sintered dual phase composite samples.

Characterization techniques. Inductively coupled plasma optical emission spectrometry (ICP-OES) analysis was used to monitor chemical composition of the dual phase ceramics by quantification of the cation content. 50 mg sample powder was mixed with 2 mL $HClO_4$ (NORMATOM®, VWR Chemicals, Germany) and heated for 30 min to fuming. After cooling, 1 mL H_2O_2 (NORMAPUR) and 1 mL HCl (Merck Suprapur, Germany) were added. Samples were heated at 70 °C for 30 min until complete dissolution of solid content and finally 50 mL volumes were prepared. Samples were measured at dilution 1:20 with a Thermo Scientific iCAP 7600 dual-view spectrometer, each sample was measured twice and the mean result of three emission lines per element was used for quantification. External calibration was performed with standards prepared by dilution of Merck Certipur® certified plasma emission standards with diluted acids. Relative standard deviation is 1–3%.

Powder X-ray diffraction (XRD) patterns of BCEO, CYO and composite BCEO:CYO as prepared and sintered were recorded in the 2 theta range from 10° to 80° using D4 ENDEAVOR diffractometer by Bruker AXS with $CuK\alpha$ radiation ($\lambda = 1.54 \text{ \AA}$). XRD patterns of BCEO:CYO membrane after permeation tests were recorded in the 2 theta range from 20° to 90° using PANalytical Cubix fast diffractometer with $CuK\alpha_{1,2}$ radiation and an X'Celerator detector in Bragg-Brentano geometry. Phase identification was carried out with ICDD PDF2-Database (Release 2004) and X'Pert Highscore Plus (by PANalytical). The TOPAS V4 software (Bruker AXS) was used to determine the lattice parameters and for Rietveld refinements. The stoichiometry of each phase

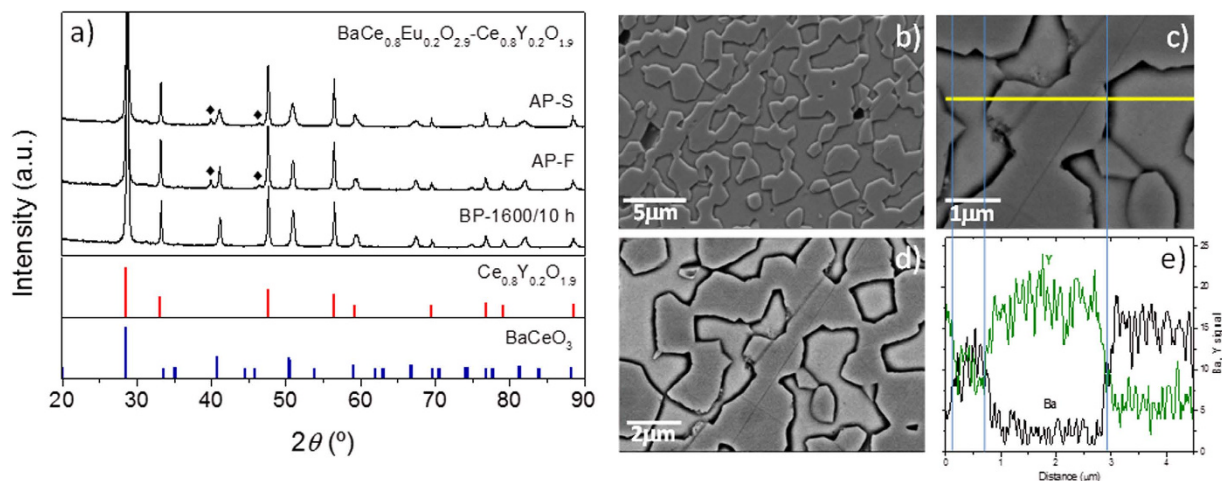


Figure 9. (a) Diffraction patterns for BCEO:CYO dual phase ceramic samples: as-sintered sample (BP-1600/10h) and sample after H_2 -permeation tests (feed side AP-F and sweep sides AP-S). Peak positions corresponding to Pt traces from the catalytic layer are denoted by symbol (\blacklozenge). As a reference (bottom): peak positions and their intensities for $BaCeO_3$ and $Ce_{0.8}Y_{0.2}O_{1.9}$. (b) SEM and (c,d) BSE-SEM micrographs and (e) EDS linescan analysis of the fractured cross-section of the BCEO:CYO membrane after the permeation measurements.

is fixed for the Rietveld refinement and the starting crystal structure model was obtained from the Inorganic Crystal Structure Database (ICSD). The final weighted R-factor (R_w, %) for each refinement is listed in Table 2.

Microstructural and chemical analyses of BCEO and CYO, as well as of the dual phase samples were performed by means of field emission scanning electron microscopy (FE-SEM) (Zeiss Ultra 55) equipped with energy-dispersive X-ray spectroscopy (EDS) (INCA, Oxford). Transmission electron microscopy (TEM) analysis was carried out using a Tecnai TF 20 UT equipped with EDS and a Gatan's imaging filter (GIF) operated at 200 kV. High-resolution scanning TEM high angle annular dark field (STEM-HAADF) imaging was performed by using C_s probe corrected FEI-Titan 80–300 STEM instrument operating at 300 kV. Electron-transparent specimens were prepared from as-sintered pellets using the traditional approach which includes ultrasonic drilling, mechanical polishing and Ar^+ ion milling at 5 keV.

Thermal expansion coefficient (TEC) of the dual phase ceramics was measured on sintered bar samples with dimensions $25 \times 4 \times 4 \text{ mm}^3$ from 30 to 1400 °C (heating rate 3 °C/min) in air using Netzsch Dil 402C. Linear thermal expansion coefficients α under heating and cooling were calculated using Eq. (2), where L_0 and dL are respectively the initial length and the length change of the sample, while T_0 and T are the starting and the final temperature, respectively:

$$\alpha = \frac{dL}{L_0(T - T_0)} \quad (2)$$

Electrical conductivity measurements were carried out by the standard four-point DC technique on sintered bars. Rectangular bar specimens were prepared from the resulting powders through uniaxial pressing at 100 MPa and subsequently sintered at 1600 °C. Silver paste and wire were used for contacting. The constant current was supplied by a programmable current source (Keithley 2601), while the voltage drop through the sample was detected by a multimeter (Keithley 3706). The voltage was measured by the current in both forward and reverse directions, in order to eliminate the thermal effect and to avoid non-ohmic responses. H/D isotopic effect and hydration effect for the separate materials and the dual phase material BCEO:CYO, were studied under reducing conditions: 5 vol.% H_2 in He and 5 vol.% D_2 in He both dry and moist (H_2 and D_2 humidified with H_2O and D_2O at room temperature, respectively). The influence of the pO_2 on total conductivity was also evaluated under wet reducing atmospheres by using: wet 0.05 vol.%, 5 vol.% and 100 vol.% H_2 and wet 5 vol.% D_2 .

Temperature-programmed reduction (TPR) was performed using 2910 Micromeritics equipment on crushed and ground samples sintered at 1600 °C. Powders were degassed under a dry Ar flow for 1 h and then were subjected to reduction under a dry H_2/Ar (1/9) flow, and a heating rate of $10^\circ\text{C}\cdot\text{min}^{-1}$ until 900 °C. H_2 consumption was measured by a TCD (thermal conductivity detector).

H_2 permeation measurements were performed in a multistep continuous process using a BCEO:CYO dense disk with a diameter of 15 mm and thickness of 500 μm sintered at 1600 °C. Both disk surfaces were coated with a 20 μm screen printed Pt porous layer aiming to improve the surface catalytic activity and evaluate predominantly the bulk H_2 transport. Permeation measurements were performed on a sealed sample in double chamber quartz reactor following the methodology reported elsewhere^{25,86}. Three different hydration conditions were evaluated: (A) feed side humidified and sweep side dry; (B) both sides humidified; (C) only sweep side humidified, where humidification means $pH_2O = 0.042 \text{ atm}$ and dry corresponds to $pH_2O = 2 \cdot 10^{-5} \text{ atm}$ (bottle dry). Ar was used as sweep gas and a 50 vol.% H_2 in He mixture was employed as feed (1.18 atm absolute pressure) under all the mentioned conditions. The flow rates used were 100 $\text{mL}\cdot\text{min}^{-1}$ for feed and 150 $\text{mL}\cdot\text{min}^{-1}$ for sweep and they

were controlled using mass flow controllers (MFCs). The hydrogen content in the permeate side was analyzed using micro-GC Varian CP-4900 equipped with Molsieve5A and PoraPlot-Q glass capillary modules. Sealing was obtained using a silver ring and applying a spring load. Sealing was confirmed by continuous monitoring the He concentration in the permeate stream and it was considered adequate when the helium concentration was lower than 5% of the H₂ permeated.

In order to evaluate the stability in operation of the composite under CO₂ containing atmospheres, H₂ permeation measurements were also performed at 700 °C for 6 days by using 15 vol.% CO₂ in Ar as sweep gas. After permeation measurements, integrity of the sample was evaluated by means of XRD and SEM analysis. Scheme of the steps of the hydrogen permeation measurements in a continuous process is given in Supplementary information, Figure S1.

Additionally, TG measurements were carried out on the BCEO, CYO and the composite BCEO:CYO by using crushed samples sintered at 1600 °C. TG was performed in a flow of dry 5% CO₂ in Ar from 25 to 1000 °C with a heating ramp of 10 K·min⁻¹ by using a Mettler-Toledo StarE balance.

References

- Meulenberg, W. A., Ivanova, M. E., Serra, J. M. & Roitsch, S. In *Advanced Membrane Science and Technology for Sustainable Energy and Environmental Applications*. 541–567 (2011).
- Sørensen, B. *Hydrogen and Fuel Cells*. (2012).
- Dincer, I. & Zamfirescu, C. *Advanced Power Generation Systems* (2014).
- Drioli, E., Stankiewicz, A. I. & Macedonio, F. Membrane engineering in process intensification-An overview. *J. Memb. Sci.* **380**, 1–8 (2011).
- Franz, J. & Scherer, V. Impact of ceramic membranes for CO₂ separation on IGCC power plant performance. *Energy Procedia* **4**, 645–652 (2011).
- Higman, C. & van der Burgt, M. In *Gasification* (Second Edition) 91–191 (Gulf Professional Publishing, 2008).
- van Holt, D. *et al.* Ceramic materials for H₂ transport membranes applicable for gas separation under coal-gasification-related conditions. *J. Eur. Cer. Soc.* **34**, 2381–2389 (2014).
- Stoukides, M. Solid-Electrolyte Membrane Reactors: Current Experience and Future Outlook. *Catal. Rev. - Science and Engineering* **42**, 1–70 (2000).
- Marnellos, G., Zisekas, S. & Stoukides, M. Synthesis of ammonia at atmospheric pressure with the use of solid state proton conductors. *J. Catal.* **193**, 80–87 (2000).
- Kjøseth, C. & Vestre, P. C. *Proton conducting membrane* (2011).
- Escolastico, S., Solis, C., Scherb, T., Schumacher, G. & Serra, J. M. Hydrogen separation in La_{5.5}WO_{11.25δ} membranes. *J. Memb. Sci.* **444**, 276–284 (2013).
- Basile, A., Gallucci, F. & Tosti, S. In *Membrane Science and Technology* Vol. 13, 255–323 (2008).
- Franz, J. & Scherer, V. An evaluation of CO₂ and H₂ selective polymeric membranes for CO₂ separation in IGCC processes. *J. Memb. Sci.* **359**, 173–183 (2010).
- Wang, N., Mundstock, A., Liu, Y., Huang, A. & Caro, J. Amine-modified Mg-MOF-74/CPO-27-Mg membrane with enhanced H₂/CO₂ separation. *Chem. Eng. Sci.* **124**, 27–36 (2015).
- Wang, N. *et al.* Polydopamine-based synthesis of a zeolite imidazolate framework ZIF-100 membrane with high H₂/CO₂ selectivity. *J. Mater. Chem. A* **3**, 4722–4728 (2015).
- Korelskiy, D. *et al.* Efficient ceramic zeolite membranes for CO₂/H₂ separation. *J. Mater. Chem. A* **3**, 12500–12506 (2015).
- Ngamou, P. H. T. *et al.* Tailoring the structure and gas permeation properties of silica membranes via binary metal oxides doping. *RSC Adv.* **5**, 82717–82725 (2015).
- Van Gestel, T., Sebald, D., Hauler, F., Meulenberg, W. A. & Buchkremer, H.-P. Potentialities of microporous membranes for H₂/CO₂ separation in future fossil fuel power plants: Evaluation of SiO₂, ZrO₂, Y₂O₃-ZrO₂ and TiO₂-ZrO₂ sol-gel membranes. *J. Memb. Sci.* **359**, 64–79 (2010).
- Kreuer, K. D. In *Annual Review of Materials Research* Vol. 33, 333–359 (2003).
- Medvedev, D. *et al.* BaCeO₃: Materials development, properties and application. *Prog. Mater. Sci.* **60**, 72–129 (2014).
- Shimura, T., Fujimoto, S. & Iwahara, H. Proton conduction in non-perovskite-type oxides at elevated temperatures. *Solid State Ionics* **143**, 117–123 (2001).
- Meulenberg, W. A. *et al.* (US Patent App. 13/810,296, 2011).
- Haugrud, R. Defects and transport properties in Ln₆WO₁₂ (Ln = La, Nd, Gd, Er). *Solid State Ionics* **178**, 555–560 (2007).
- Seeger, J. *et al.* Synthesis and Characterization of Nonsubstituted and Substituted Proton-Conducting La_{6-x}WO_{12-y}. *Inorg Chem* **52**, 10375–10386 (2013).
- Escolastico, S. *et al.* Enhanced H₂ separation through mixed proton-electron conducting membranes based on La_{5.5}W_{0.8}Mo_{0.2}O_{11.25-δ}. *ChemSusChem* **6**, 1523–1532 (2013).
- Deibert, W., Ivanova, M. E., Meulenberg, W. A., Vaßen, R. & Guillon, O. Preparation and sintering behaviour of La_{5.4}WO_{12-δ} asymmetric membranes with optimised microstructure for hydrogen separation. *J. Memb. Sci.* **492**, 439–451 (2015).
- Phair, J. W. & Badwal, S. P. S. Review of proton conductors for hydrogen separation. *Ionics* **12**, 103–115 (2006).
- Haugrud, R. & Norby, T. Proton conduction in rare-earth ortho-niobates and ortho-tantalates. *Nat. Mater.* **5**, 193–196 (2006).
- Mather, G. C., Fisher, C. A. J. & Islam, M. S. Defects, dopants, and protons in LaNbO₄. *Chem. Mater.* **22**, 5912–5917 (2010).
- Mokkelbost, T. *et al.* High-temperature proton-conducting lanthanum ortho-niobate-based materials. Part II: Sintering properties and solubility of alkaline earth oxides. *J. Amer. Ceram. Soc.* **91**, 879–886 (2008).
- Ivanova, M. E. *et al.* Functional properties of La_{0.99}X_{0.01}Nb_{0.99}Al_{0.01}O_{4-δ} and La_{0.99}X_{0.01}Nb_{0.99}Ti_{0.01}O_{4-δ} proton conductors where X is an alkaline earth cation. *J. Eur. Ceram. Soc.* **35**, 1239–1253 (2015).
- Huse, M., Norby, T. & Haugrud, R. Proton conductivity in acceptor-doped LaVO₄. *J. Electrochem. Soc.* **158** (2011).
- Ivanova, M. *et al.* In *Doping: Properties, Mechanisms and Applications* 221–276 (2013).
- Escolastico, S., Vert, V. B. & Serra, J. M. Preparation and Characterization of Nanocrystalline Mixed Proton-Electronic Conducting Materials Based on the System Ln₆WO₁₂. *Chem. Mater.* **21**, 3079–3089 (2009).
- Escolastico, S., Solis, C. & Serra, J. M. Hydrogen separation and stability study of ceramic membranes based on the system Nd₅LnWO₁₂. *Int J Hydrogen Energy* **36**, 11946–11954 (2011).
- Escolastico, S., Solis, C. & Serra, J. M. Study of hydrogen permeation in (La_{5/6}Nd_{1/6})_{5.5}WO_{12-δ} membranes. *Solid State Ionics* **216**, 31–35 (2012).
- Escolastico, S., Somacescu, S. & Serra, J. M. Tailoring mixed ionic-electronic conduction in H₂ permeable membranes based on the system Nd_{5.5}W_{1-x}Mo_xO_{11.25-σ}. *J. Mater. Chem. A* **3**, 719–731 (2015).
- Escolastico, S., Somacescu, S. & Serra, J. M. Solid State Transport and Hydrogen Permeation in the System Nd_{5.5}W_{1-x}Re_xO_{11.25-δ}. *Chem. Mater.* **26**, 982–992 (2014).

39. Matsumoto, H. *et al.* Protonic-electronic mixed conduction and hydrogen permeation in $\text{BaCe}_{0.9-x}\text{Y}_{0.1}\text{Ru}_x\text{O}_{3-\alpha}$. *J. Electrochem. Soc.* **152** (2005).
40. Cai, M. *et al.* Preparation and hydrogen permeation of $\text{BaCe}_{0.95}\text{Nd}_{0.05}\text{O}_{3-\delta}$ membranes. *J. Memb. Sci.* **343**, 90–96 (2009).
41. Escolastico, S. *et al.* Improvement of transport properties and hydrogen permeation of chemically-stable proton-conducting oxides based on the system $\text{BaZr}_{1-x}\text{Y}_x\text{M}_x\text{O}_{3-\delta}$. *RSC Adv.* **2**, 4932–4943 (2012).
42. Cheng, S. G., Gupta, V. K. & Lin, J. Y. S. Synthesis and hydrogen permeation properties of asymmetric proton-conducting ceramic membranes. *Solid State Ionics* **176**, 2653–2662 (2005).
43. Qi, X. W. & Lin, Y. S. Electrical conduction and hydrogen permeation through mixed proton-electron conducting strontium cerate membranes. *Solid State Ionics* **130**, 149–156 (2000).
44. Kniep, J. & Lin, Y. S. Effect of Zirconium Doping on Hydrogen Permeation through Strontium Cerate Membranes. *Ind. Eng. Chem. Res.* **49**, 2768–2774 (2010).
45. Wei, X., Kniep, J. & Lin, Y. S. Hydrogen permeation through terbium doped strontium cerate membranes enabled by presence of reducing gas in the downstream. *J. Memb. Sci.* **345**, 201–206 (2009).
46. Zhan, S. *et al.* Preparation and hydrogen permeation of $\text{SrCe}_{0.95}\text{Y}_{0.05}\text{O}_{3-\delta}$ asymmetrical membranes. *J. Memb. Sci.* **340**, 241–248 (2009).
47. Hamakawa, S., Li, L., Li, A. & Iglesia, E. Synthesis and hydrogen permeation properties of membranes based on dense $\text{SrCe}_{0.95}\text{Yb}_{0.05}\text{O}_{3-\alpha}$ thin films. *Solid State Ionics* **148**, 71–81 (2002).
48. Song, S. J., Wachsman, E. D., Rhodes, J., Dorris, S. E. & Balachandran, U. Hydrogen permeability of $\text{SrCe}_{1-x}\text{M}_x\text{O}_{3-\delta}$ ($x = 0.05$, $\text{M} = \text{Eu}$, Sm). *Solid State Ionics* **167**, 99–105 (2004).
49. Liang, J., Mao, L., Li, L. & Yuan, W. Protonic and Electronic Conductivities and Hydrogen Permeation of $\text{SrCe}_{0.95-x}\text{Zr}_x\text{Tm}_{0.05}\text{O}_{3-\delta}$ ($0 < x < 0.40$) Membrane. *Chinese J. Chem. Eng.* **18**, 506–510 (2010).
50. Xing, W. *et al.* Hydrogen permeability of $\text{SrCe}_{0.7}\text{Zr}_{0.25}\text{Ln}_{0.05}\text{O}_{3-\delta}$ membranes ($\text{Ln} = \text{Tm}$ and Yb). *J. Memb. Sci.* **473**, 327–332 (2015).
51. Oh, T., Yoon, H., Li, J. & Wachsman, E. D. Hydrogen permeation through thin supported $\text{SrZr}_{0.2}\text{Ce}_{0.8-x}\text{Eu}_x\text{O}_{3-\delta}$ membranes. *J. Memb. Sci.* **345**, 1–4 (2009).
52. Meng, X. *et al.* Ni-Ba $\text{Ce}_{0.95}\text{Tb}_{0.05}\text{O}_{3-\delta}$ cermet membranes for hydrogen permeation. *J. Memb. Sci.* **401**, 300–305 (2012).
53. Kim, H. *et al.* Microstructural adjustment of Ni-Ba $\text{Ce}_{0.9}\text{Y}_{0.1}\text{O}_{3-\delta}$ cermet membrane for improved hydrogen permeation. *Ceram. Int.* **40**, 4117–4126 (2014).
54. Song, S. J., Moon, J. H., Lee, T. H., Dorris, S. E. & Balachandran, U. Thickness dependence of hydrogen permeability for Ni-Ba $\text{Ce}_{0.8}\text{Y}_{0.2}\text{O}_{3-\delta}$. *Solid State Ionics* **179**, 1854–1857 (2008).
55. Wei, Y. *et al.* Enhanced stability of Zr-doped Ba(CeTb) $\text{O}_{3-\delta}$ -Ni cermet membrane for hydrogen separation. *Chem. Comm.* **51**, 11619–11621 (2015).
56. Zuo, C., Dorris, S. E., Balachandran, U. & Liu, M. Effect of Zr-doping on the chemical stability and hydrogen permeation of the Ni-Ba $\text{Ce}_{0.8}\text{Y}_{0.2}\text{O}_{3-\alpha}$ mixed protonic-electronic conductor. *Chem. Mater.* **18**, 4647–4650 (2006).
57. Fang, S., Brinkman, K. S. & Chen, F. Hydrogen permeability and chemical stability of Ni-Ba $\text{Zr}_{0.1}\text{Ce}_{0.7}\text{Y}_{0.1}\text{Yb}_{0.1}\text{O}_{3-\delta}$ membrane in concentrated H_2O and CO_2 . *J. Memb. Sci.* **467**, 85–92 (2014).
58. Fang, S. *et al.* CO_2 -Resistant Hydrogen Permeation Membranes Based on Doped Ceria and Nickel. *J. Phys. Chem. C* **114**, 10986–10991 (2010).
59. Balachandran, U. *et al.* Dense cermet membranes for hydrogen separation. *Sep. Purif. Technol.* **121**, 54–59 (2014).
60. Escolastico, S., Solis, C., Kjolseth, C. & Serra, J. M. Outstanding hydrogen permeation through CO_2 -stable dual-phase ceramic membranes. *Energ Environ Sci* **7**, 3736–3746 (2014).
61. Elangovan, S., Nair, B. G. & Small, T. A. Ceramic mixed protonic/electronic conducting membranes for hydrogen separation. (2007).
62. Rosensteel, W. A., Ricote, S. & Sullivan, N. P. Hydrogen permeation through dense Ba $\text{Ce}_{0.8}\text{Y}_{0.2}\text{O}_{3-\delta}$ -Ce $\text{O}_{0.8}\text{Y}_{0.2}\text{O}_{2-\delta}$ composite-ceramic hydrogen separation membranes. *Int J Hydrogen Energy* **41**, 2598–2606 (2016).
63. Rebollo, E. *et al.* Exceptional hydrogen permeation of all-ceramic composite robust membranes based on Ba $\text{Ce}_{0.65}\text{Zr}_{0.20}\text{Y}_{0.15}\text{O}_{3-\delta}$ and Y- or Gd-doped ceria. *Energ Environ Sci* **8**, 3675–3686 (2015).
64. Fish, J. S., Ricote, S., O'Hayre, R. & Bonanos, N. Electrical properties and flux performance of composite ceramic hydrogen separation membranes. *J. Mater. Chem. A* **3**, 5392–5401 (2015).
65. Unemoto, A. *et al.* Hydrogen permeability and electrical properties in oxide composites. *Solid State Ionics* **178**, 1663–1667 (2008).
66. Scholten, M. J., Schoonman, J., Vanmiltenburg, J. C. & Oonk, H. A. J. Synthesis of Strontium and Barium Cerate and Their Reaction with Carbon-Dioxide. *Solid State Ionics* **61**, 83–91 (1993).
67. Dauter, J., Maffei, N., Bhella, S. S. & Thangadurai, V. Studies on Chemical Stability and Electrical Properties of Proton Conducting Perovskite-Like Doped Ba CeO_3 . *J. Electrochem. Soc.* **157**, B1413–B1418 (2010).
68. Brandao, A. *et al.* Guidelines for improving resistance to CO_2 of materials for solid state electrochemical systems. *Solid State Ionics* **192**, 16–20 (2011).
69. Matsumoto, H., Shimura, T., Yogo, T., Iwahara, H. & Katahira, K. (Google Patents, 2003).
70. Ricote, S., Manerbin, A., Sullivan, N. P. & Coors, W. G. Preparation of dense mixed electron- and proton-conducting ceramic composite materials using solid-state reactive sintering: Ba $\text{Ce}_{0.8}\text{Y}_{0.1}\text{M}_{0.1}\text{O}_{3-\delta}$ -Ce $\text{O}_{0.8}\text{Y}_{0.1}\text{M}_{0.1}\text{O}_{2-\delta}$ ($\text{M} = \text{Y}$, Yb , Er , Eu). *J. Mater. Sci.* **49**, 4332–4340 (2014).
71. Medvedev, D. *et al.* Structural, thermomechanical and electrical properties of new $(1-x)\text{Ce}_{0.8}\text{Nd}_{0.2}\text{O}_{2-\delta}$ - $x\text{BaCe}_{0.8}\text{Nd}_{0.2}\text{O}_{3-\delta}$ composites. *J. Power Sources* **267**, 269–279 (2014).
72. Huang, J., Zhang, L., Wang, C. & Zhang, P. CYO-BZCYO composites with enhanced proton conductivity: Candidate electrolytes for low-temperature solid oxide fuel cells. *Int J Hydrogen Energy* **37**, 13044–13052 (2012).
73. Ryu, K. H. & Haile, S. M. Chemical stability and proton conductivity of doped Ba CeO_3 -Ba ZrO_3 solid solutions. *Solid State Ionics* **125**, 355–367 (1999).
74. Matskevich, N. I. & Wolf, T. A. The enthalpies of formation of Ba $\text{Ce}_{1-x}\text{RE}_x\text{O}_{3-\delta}$ ($\text{RE} = \text{Eu}$, Tb , Gd). *J. Chem. Thermodyn.* **42**, 225–228 (2010).
75. Amsif, M. *et al.* Influence of rare-earth doping on the microstructure and conductivity of Ba $\text{Ce}_{0.9}\text{Ln}_{0.1}\text{O}_{3-\delta}$ proton conductors. *J. Power Sources* **196**, 3461–3469 (2011).
76. Bonanos, N., Ellis, B., Knight, K. S. & Mahmood, M. N. Ionic-conductivity of gadolinium-doped barium cerate perovskites. *Solid State Ionics* **35**, 179–188 (1989).
77. Wachsman, E. D. & Jiang, N. Ionic conductor useful as hydrogen gas permeation membrane or electrode material comprises a perovskite-type oxide. EP1048613-A1; CA2307005-A1; US2001001379-A1; US6296687-B2; EP1048613-B1; DE60020772-E; DE60020772-T2; CA2307005-C.
78. Radojkovic, A. *et al.* Structural and electrical properties of Ba $\text{Ce}_{0.9}\text{Eu}_{0.1}\text{O}_{2.95}$ electrolyte for IT-SOFCs. *Electrochimica Acta* **161**, 153–158 (2015).
79. Kim, D.-J. Lattice Parameters, Ionic Conductivities, and Solubility Limits in Fluorite-Structure MO_2 Oxide [$\text{M} = \text{Hf}^{4+}$, Zr^{4+} , Ce^{4+} , Th^{4+} , U^{4+}] Solid Solutions. *J. Amer. Ceram. Soc.* **72**, 1415–1421 (1989).
80. Guan, X., Zhou, H., Wang, Y. & Zhang, J. Preparation and properties of Gd^{3+} and Y^{3+} co-doped ceria-based electrolytes for intermediate temperature solid oxide fuel cells. *J. Alloy. Compd.* **464**, 310–316 (2008).
81. Wang, S. R., Kobayashi, T., Dokiya, M. & Hashimoto, T. Electrical and ionic conductivity of Gd-doped ceria. *J. Electrochem. Soc.* **147**, 3606–3609 (2000).

82. Balaguer, M., Solis, C., Roitsch, S. & Serra, J. M. Engineering microstructure and redox properties in the mixed conductor $\text{Ce}_{0.9}\text{Pr}_{0.1}\text{O}_{2-\delta} + \text{Co}$ 2 mol%. *Dalton Transactions* **43**, 4305–4312 (2014).
83. Escolastico, S., Schroeder, M. & Serra, J. M. Optimization of the mixed protonic-electronic conducting materials based on $(\text{Nd}_{5/6}\text{Ln}_{1/6})_{5.5}\text{WO}_{11.25-\delta}$. *J. Mater. Chem. A* **2**, 6616–6630 (2014).
84. Balaguer, M., Solis, C. & Serra, J. M. Structural-Transport Properties Relationships on $\text{Ce}_{1-x}\text{Ln}_x\text{O}_{2-\delta}$ System (Ln = Gd, La, Tb, Pr, Eu, Er, Yb, Nd) and Effect of Cobalt Addition. *J. Phys. Chem. C* **116**, 7975–7982 (2012).
85. Escolastico, S., Kjøselth, C. & Serra, J. M. Catalytic activation of ceramic H_2 membranes for CMR processes. *J. Memb. Sci.* **517**, 57–63 (2016).
86. Escolastico, S. & Serra, J. M. $\text{Nd}_{5.5}\text{W}_{1-x}\text{U}_x\text{O}_{11.25-\delta}$ system: Electrochemical characterization and hydrogen permeation study. *J. Memb. Sci.* **489**, 112–118 (2015).

Acknowledgements

This work has been conducted with the financial support by the Helmholtz Association under the Research Programme *Energy Efficiency, Materials and Resources*. Financial funding from the Spanish Government (ENE2014-57651 and SEV-2012-0267 grants) is also gratefully acknowledged. ZEA-3 at FZJ is gratefully acknowledged for performing the ICP-OES analysis.

Author Contributions

M.E.I., W.A.M., O.G., S.E. and J.M.S. designed the project and lead the interpretation and writing of the manuscript. M.E.I. and S.E. performed the electrochemical measurements. J.P. and J.M. carried out the microstructural analysis, Y.J.S. and M.B. contributed to the structural characterization. All authors contributed to the concept and analysis of results, and revised the manuscript.

Additional Information

Supplementary information accompanies this paper at <http://www.nature.com/srep>

Competing financial interests: The authors declare no competing financial interests.

How to cite this article: Ivanova, M. E. *et al.* Hydrogen separation through tailored dual phase membranes with nominal composition $\text{BaCe}_{0.8}\text{Eu}_{0.2}\text{O}_{3-\delta}:\text{Ce}_{0.8}\text{Y}_{0.2}\text{O}_{2-\delta}$ at intermediate temperatures. *Sci. Rep.* **6**, 34773; doi: 10.1038/srep34773 (2016).

Publisher's note: Springer Nature remains neutral with regard to jurisdictional claims in published maps and institutional affiliations.



This work is licensed under a Creative Commons Attribution 4.0 International License. The images or other third party material in this article are included in the article's Creative Commons license, unless indicated otherwise in the credit line; if the material is not included under the Creative Commons license, users will need to obtain permission from the license holder to reproduce the material. To view a copy of this license, visit <http://creativecommons.org/licenses/by/4.0/>

© The Author(s) 2016